INTERNATIONAL JOURNAL FOR NUMERICAL METHODS IN FLUIDS
*Int. J. Numer. Meth. Fluids* 2006; **50**:1229–1246
Published online 28 December 2005 in Wiley InterScience (www.interscience.wiley.com). DOI: 10.1002/fld.1138

# Numerical simulation of sand dune evolution in severe winds

Pablo Ortiz[1] and Piotr K. Smolarkiewicz[2,*,†]

[1]*University of Granada, Ed. Politecnico, Campus Fuentenueva, Granada 18071, Spain*
[2]*National Center for Atmospheric Research, Boulder, CO 80307, U.S.A.*

SUMMARY

We present a novel approach for numerical simulation of fluid flow and sediment transport past evolutionary landforms, with emphasis on sand dunes developing in extreme winds. Time-dependent curvilinear coordinates are employed to fully couple flow aloft with the developing landform. The conservation law that defines shape of the lower boundary depends on details of local surface stress, thereby favouring a large eddy simulation of the atmospheric boundary layer. The flux-form partial differential equation for the interface profile—via saltation and sand avalanches—is formulated as an advection–diffusion equation. The latter facilitates discrete integrations using nonoscillatory algorithms—consistent with the nonoscillatory forward-in-time solver, based on MPDATA transport methods, employed to simulate the boundary layer flow aloft. Theoretical discussions are illustrated with numerical experiments that explore the interactive evolution of the dune/atmosphere system. Copyright © 2005 John Wiley & Sons, Ltd.

KEY WORDS: modelling sand dunes; saltation; sand avalanches; boundary layer sand dune coupling

## 1. INTRODUCTION

Fluid flows and accompanying cohesionless sediment transport over evolutionary landforms is a fundamental dynamical mechanism with challenging details. Whenever the landform plays an active role in determining both the fluid flow and the sediment motion—e.g. when erosion and sedimentation mould the landform, modifying in turn the flow aloft—the underlying dynamics amount to flows with intricate geometric time-dependent boundary forcing. Among the variety of active landforms, evolutionary dunes are an archetype of fluid/terrain interaction. Diagnosis and prediction of dune development and accompanying sand transport is important for environmental research and engineering, in areas such as the desertification processes, beach erosion, or conservation of trafficability in arid regions.

In the research of sand dunes, relatively little work has been devoted to the coupled dune/fluid system. The two-phase interaction is typically neglected [1–4], or simplified

*Correspondence to: Piotr K. Smolarkiewicz, National Center for Atmospheric Research, Boulder, CO 80307, U.S.A.
†E-mail: smolar@ucar.edu

Contract/grant sponsor: U.S. Department of Energy

*Received 25 March 2005*
*Revised 12 August 2005*
*Accepted 20 October 2005*

adopting a quasi-steady approximation (QSA). The QSA assumes a time scale of flow variability much shorter than of the dune evolution, so that the modelled dune evolution depends parametrically on the boundary layer flow. For example, numerical simulations of barchan and transverse dunes [5, 6] employ surface shear stresses provided by a semi-analytic solution of a steady-state boundary layer model for 3D flows past fixed hills. Whereas, calculations of Wippermann and Gross [7] integrate the flow equations past a frozen landform to a steady state, and update the boundary profile subsequently in the frozen flow—in the spirit of the classical Achilles–Turtle iteration.

Although solutions generated with the steady and QSA models capture many qualitative aspects of dune evolution and shed light on dune dynamics [1, 6], there are outstanding issues lacking either satisfactory understanding or quantification. Examples include the attainability of the equilibrium shape of an isolated barchan dune [5, 7], calving barchan dunes [1], estimating the rates of erosion [5], and details of the genesis and development of barchan dunes [7]. The fundamental role of the wind velocity field in dune evolution, and its oversimplification in contemporary models are often acknowledged [5, 6, 8–10]. Obviously, the assumption of scale separation that underlies QSA models cannot be generally valid. For counterexample, consider dune evolution in extreme winds, an event familiar from the popular literature and cinema. Moreover, scale analysis is only discriminating when it identifies processes that cannot be neglected. Since dune/fluid dynamics is governed by complex nonlinear PDEs, even small-magnitude terms can have a profound impact on the solution. Consequently, the effect of QSA on the generated solutions remains unclear.

In this work, we adopt a 'severe wind scenario', relax the limitations of the quasi-steady approximation, and fully couple the two phases of the dune/fluid system. We employ a variant of the nonhydrostatic atmospheric numerical model EULAG—a broadly documented in the literature high-performance flow solver based on the MPDATA schemes [11]—that couples the internal flow with a lower boundary evolving in response to the sand saltation. The key feature of the EULAG model is the use of time-dependent curvilinear coordinate transformation [12–16] that accommodates rapid changes of the boundary shape. Due to the adopted severe wind scenario, the geometric difficulty of the two-phase coupling is enhanced by the ubiquity of the turbulence and separating boundary layer. Since a realistic response of the sediment-transport model depends crucially on the formulation of the boundary stress, we employ a large-eddy-simulation (LES) approach with the Smagorinsky-type subgrid-scale turbulence model [17].

The locus of the solid/fluid interface is standardly described by a differential conservation law relating the height of the interface to the divergence of sediment fluxes [5, 7, 18]. Following the MPDATA approach,[‡] we cast the standard equation in an advection–diffusion PDE form, to improve the solution accuracy while simplifying the computational procedures. In particular, the saltation fluxes—assumed dominant for the landform development—are written as convective fluxes, with the effective velocity representing the transport rate averaged over the local thickness of the sediment stratum. In contrast, the sand avalanches—acting as natural slope limiter—are represented as diffusive fluxes with an anisotropic, inhomogeneous diffusion coefficient depending critically on the local slope, cf. Reference [19]. With the

[‡]In essence, MPDATA relies on transforming PDEs into forms more convenient for computing; cf. Reference [11] and references therein.

 

rearranged sediment conservation law, the nonoscillatory forward-in-time numerical technology of EULAG improves the accuracy, stability, and robustness of earlier approximations. We verify the theoretical developments by canonical experiments addressing the dynamics of barchan dunes, with a solid ground or erodible bed underneath the initial sand pile.

The remainder of the paper is organized as follows. In the following section, the theoretical formulation of our two-phase dune/fluid dynamics model is outlined. The numerical approximations to PDEs governing both phases of the model are presented in Section 3. Design of numerical experiments and the corresponding results are discussed in Section 4. Remarks in Section 5 conclude the paper.

## 2. THEORETICAL FORMULATION

### 2.1. Fluid model

The nonhydrostatic anelastic model EULAG used in this study has been broadly documented in the literature; see References [13–15] for recent developments and reviews. Here, we consider shallow flows of a thermally homogeneous planetary boundary layer, and adopt the classical incompressible Boussinesq approximation in the governing fluid equations. Consequently, we invoke only a small portion of the model's capabilities, thereby simplifying the presentation as well as computational procedures. The scope of this paper justifies a concise, operator-like symbolic description of the governing equations. Wherever the operator symbols refer to coefficient matrices, they merely indicate matrix operations but do not follow the formalism of matrix algebra to the letter—for a thorough mathematical expositions refer to References [13–16].

To address a broad class of flows in a variety of domains, the governing equations are formulated (and solved) in transformed time-dependent curvilinear coordinates

$$(\bar{t},\ \bar{\mathbf{x}}) \equiv (t, \mathscr{F}(t, \mathbf{x})) \tag{1}$$

with assumptions that the coordinates $(t, \mathbf{x})$ of the physical domain are orthogonal and stationary—in particular, Cartesian in this paper—and the transformed horizontal coordinates $(\bar{x}, \bar{y})$ are independent of the vertical coordinate $z$. Given the transformation in (1), the incompressible Boussinesq equations for neutrally stratified flow can be compactly written as follows:

$$\bar{\nabla} \bullet (\rho^* \bar{\mathbf{v}}^s) = 0 \tag{2}$$

$$\frac{\mathrm{d}\mathbf{v}}{\mathrm{d}\bar{t}} = -\tilde{\mathbf{G}}\,\bar{\nabla}\pi' + \mathbf{D} \tag{3}$$

where, because of the coordinate transformation, the physical and geometrical aspects are intertwined. Insofar as the physics is concerned: $\mathbf{v}$ denotes the *physical velocity* vector; $\rho$ and $\pi$ denote density and a density-normalized pressure, respectively; $\mathbf{D}$ symbolizes viscous dissipation of momentum via divergence of turbulent stresses. Primes denote deviations from the static ambient state, characterized by uniform density $\rho_o$.

The geometry of the coordinates in (1) enters the governing equations as follows: in the mass continuity equation (2), $\rho^* \equiv \rho_o \bar{G}$ with $\bar{G}$ denoting the Jacobian of the transformation; whereas in the momentum equation (3), $\tilde{\mathbf{G}} \sim (\partial\,\bar{\mathbf{x}}/\partial\mathbf{x})$ symbolizes the renormalized Jacobi

 

matrix of the transformation coefficients; $\bar{\nabla} \bullet \equiv \partial/\partial \bar{\mathbf{x}} \bullet$, and the total derivative is given by $\mathrm{d}/\mathrm{d}\bar{t} = \partial/\partial\bar{t} + \bar{\mathbf{v}}^* \bullet \bar{\nabla}$, where $\bar{\mathbf{v}}^* \equiv \mathrm{d}\,\bar{\mathbf{x}}/\mathrm{d}\bar{t} \equiv \dot{\bar{\mathbf{x}}}$ is the *contravariant velocity*. Appearing in the continuity equation (2) is the *solenoidal velocity*

$$\bar{\mathbf{v}}^{\mathrm{s}} \equiv \bar{\mathbf{v}}^* - \frac{\partial\,\bar{\mathbf{x}}}{\partial t} \tag{4}$$

that follows, see Reference [20], from the generic (tensor invariant) form of incompressible continuity equation

$$\bar{G}^{-1}\left(\frac{\partial \rho^*}{\partial \bar{t}} + \bar{\nabla} \bullet (\rho^* \bar{\mathbf{v}}^*)\right) \equiv 0 \tag{5}$$

The transformation

$$\bar{\mathbf{v}}^{\mathrm{s}} = \tilde{\mathbf{G}}^{\mathrm{T}} \mathbf{v} \tag{6}$$

relates the solenoidal and physical velocities directly. For further details of the metric and transformation tensors as well as formulating viscous and dissipative terms in the governing equations, the interested reader is referred to Reference [15] and the references therein.

Following Reference [14], the general dependence of $\bar{z}$ on $(x, y, z, t)$ in (1) collapses into a similarity transformation

$$\begin{aligned} \bar{z} &= \mathscr{C}(\xi) \\ \xi &= \xi(x, y, z, t) := H_0 \frac{z - z_{\mathrm{s}}(x, y, t)}{H(x, y, t) - z_{\mathrm{s}}(x, y, t)} \end{aligned} \tag{7}$$

with the inverse relationship

$$\begin{aligned} z &= \frac{\xi}{H_0}(H - z_{\mathrm{s}}) + z_{\mathrm{s}} \\ \xi &= \mathscr{C}^{-1}(\bar{z}) \end{aligned} \tag{8}$$

Here $H$ and $z_{\mathrm{s}}$ are the upper and lower surface elevations, respectively, $H_0$ denotes the vertical extend of the transformed model domain, and the function $\mathscr{C}$ conveniently admits a class of vertically stretched coordinates. The transformation in (7) has the computational advantage of separability into one- and two-dimensional fields. In particular, the Jacobian of the transformation is given as

$$\begin{aligned} \bar{G} &= \left(\frac{\mathrm{d}\mathscr{C}}{\mathrm{d}\xi}\frac{\partial \xi}{\partial z}\right)^{-1}\left(\frac{\partial \bar{x}}{\partial x}\frac{\partial \bar{y}}{\partial y} - \frac{\partial \bar{x}}{\partial y}\frac{\partial \bar{y}}{\partial x}\right)^{-1} \\ &\equiv \left(\frac{\mathrm{d}\mathscr{C}}{\mathrm{d}\xi}\right)^{-1} \bar{G}_0 \bar{G}_{xy} \end{aligned} \tag{9}$$

 

with

$$\bar{G}_0 \equiv \left(\frac{\partial \xi}{\partial z}\right)^{-1} = \frac{H(x,y,t) - z_s(x,y,t)}{H_0} \tag{10}$$

Throughout this paper, $\bar{x} = x$, $\bar{y} = y$ and $\xi = \bar{z}$; thereby employing the identity transformation in the horizontal (viz. $\bar{G}_{xy} \equiv 1$). Furthermore, the upper boundary is stationary and flat (viz. $H \equiv H_0$), and there is no vertical stretching of the lower-boundary-fitted coordinate $\bar{z}$ (viz. $\mathrm{d}\mathscr{C}/\mathrm{d}\xi \equiv 1$). However, since all reported mathematical and numerical developments accommodate (1) and (7) in their full generality, we retain the consistent notation, for future reference.

Our mathematical framework enables the specification of the lower surface by arbitrary means (either approximated or exactly prescribed). Here, we drive the time-dependent transformation (7) by the solution of the sediment motion model—discussed next—such that $z_s \equiv h$, where $h$ is the solid/fluid interface profile.

### 2.2. Sediment motion

The evolution of the solid/fluid interface is governed by the mass conservation law

$$\rho_s \frac{\partial h}{\partial t} + \nabla_H \bullet \mathbf{q} = 0 \tag{11}$$

where $\rho_s = \rho_m(1 - \lambda)$ is the bulk density of the sediment with $\rho_m$ and $\lambda$ denoting, respectively, the density of the grain material and the porosity (volume of voids/total volume); $\nabla_H$ symbolizes the horizontal nabla operator of the physical space; and $\mathbf{q}$ is a vertically integrated sediment mass flux.

In usual aeolian transport, where sand is the prevailing fraction of the grain mixture, the sediment flux $\mathbf{q}$ is ascribed to the saltation. Saltation includes particle-size scale processes such as the direct momentum transfer from the fluid to the grains (drag), aerodynamic entrainment, and ejection due to grain collisions (splash) [18]. The saltation flux $\mathbf{q}_S$ follows the Bagnold law [21] of the *saturation* condition,[§] adjusted to account for the critical dependence of the saltation transport on the friction velocity and variable flow direction [7, 23]. In the resulting formula

$$\mathbf{q}_S = C\frac{\rho}{g}\mathbf{u}_*\|\mathbf{u}_*\|^2 \max\left(0, 1 - \frac{u_\tau}{\|\mathbf{u}_*\|}\right) \tag{12}$$

we adopt the following notation: $C$ is an empirical coefficient depending (to a first approximation [24]) upon the square root of normalized grain size; $\rho$ is the density of the air; $g = |\mathbf{g}|$, where $\mathbf{g}$ is the acceleration of gravity; $\mathbf{u}_* \equiv u_*\mathbf{v}\|\mathbf{v}\|^{-1}$, where the friction velocity $u_* = \sqrt{\rho^{-1}\tau_w}$; while $\tau_w$ and $u_\tau$ denote the wall shear stress and threshold value of $u_*$, respectively.

In general, the threshold friction velocity $u_\tau$ depends on the landform slope [25]. In 3D, however, local flow does not necessarily align with the maximum slope. In order to correct for the misalignment, we have developed a generalized formula for $u_\tau$ (see Appendix A).

[§]The saturation condition is defined by the equilibrated momentum transfer from the air to the grains; for alternative prognostic constitutive modelling of saltation, that relaxes the saturation assumption, see References [18, 22].

 

Figure 1. Local sand avalanches beneath the brink of a dune.

Following Reference [26], where shear stresses in curved trapezoidal channels were addressed, we assumed the equality of tractive force and friction, and drag coefficient independent of the slope magnitude. The resulting formula relates the actual threshold velocity to the threshold friction velocity $u_{\tau 0}$ for a flat bed,¶

$$u_\tau = \sqrt{\frac{\sin\theta}{\tan\alpha}\cos\gamma + \sqrt{\frac{\sin^2\theta}{\tan^2\alpha}(\cos^2\gamma - 1) + \cos^2\theta}\, u_{\tau 0}} \tag{13}$$

where $\theta$ is the local slope angle, $\alpha$ is the angle of friction, and $\gamma$ is the angle between local wind and slope. For the special case of $\gamma = 0$, (13) reduces to Equation (5) in Reference [25].

The saltation flux alone is insufficient for representing realistic dune development. Similar to pile surface dynamics [19], sand dunes are subject to self-organized criticality [28, 29], where upon reaching the critical slope ($s_C \equiv \tan\alpha = 0.625$ for sand) local grain avalanches discharge particle steepest descent to stabilize the slope. For illustration, we show in Figure 1 the photograph we took in the Great Sand Dunes National Park, Colorado. It conveys particularly well the scale disparity of the sand avalanches and dunes; cf. References [7, 24] for discussions. In our formulation of the coupled flow/sediment-transport problem, accounting for the avalanches is essential, since otherwise unbounded steepening of local slopes leads to a singularity of the transformation in (7).

¶ Values of $u_{\tau 0}$ for various soil particles can be found in Reference [27].

 

Following Reference [19], we represent the avalanche transport in the form of diffusion fluxes, with an anisotropic, inhomogeneous diffusion coefficient depending critically on the local slope

$$\mathbf{q}_{\mathrm{A}} = -\rho_{\mathrm{s}} \mathscr{K} \nabla_{\mathrm{H}} h \tag{14}$$

Here $\mathscr{K}(\mathbf{x}, t)|_{\bar{z}=0}$ is the associated diffusion coefficient, defined as

$$\mathscr{K} := \frac{\Lambda^2}{\Upsilon} \frac{1 + \mathrm{sgn}(\|\nabla_{\mathrm{H}} h\| - s_{\mathrm{C}})}{2} \tag{15}$$

where $\Lambda$ and $\Upsilon$ denote the characteristic length and time scales (yet to be specified).

The total flux entering the mass conservation law (11) is a sum of $\mathbf{q}_{\mathrm{S}}$ and $\mathbf{q}_{\mathrm{A}}$. To aid in understanding of dune propagation as well as to facilitate the solution procedures, we cast (11) in the form of an advection–diffusion equation

$$\frac{\partial h}{\partial t} + \nabla_{\mathrm{H}} \bullet \mathbf{U} h = \nabla_{\mathrm{H}} \bullet \mathscr{K} \nabla_{\mathrm{H}} h \tag{16}$$

with the advective velocity $\mathbf{U}$ defined as

$$\mathbf{U} := \frac{\mathbf{q}_{\mathrm{S}}}{\rho_s h} \tag{17}$$

Formally, (16) is equivalent to (11) for any $h = h'(\mathbf{x}, t) + \mathrm{const}$, since the singularity of $\mathbf{U}$, as $h \searrow 0$, is removable. In order to give $\mathbf{U}$ a unique physical interpretation, we define $h$ with respect to horizontal reference level at the upper limit of nonerodible substrate. Hence, $\mathbf{U}$ is an average velocity over a potentially mobilized sand layer.

Mathematically, the advection diffusion equation (16) can be viewed as a special case of the equations of motion—here, (2) and (3)—discussed thoroughly in References [13–15]. Consequently, the mathematical apparatus developed therein applies readily, resulting in the transformed form of (16)

$$\frac{\partial \bar{G}_{xy} h}{\partial \bar{t}} + \bar{\nabla}_{\mathrm{H}} \bullet (\bar{G}_{xy} \bar{\mathbf{U}}^* h) = \bar{\nabla}_{\mathrm{H}} \bullet (\mathscr{K} \bar{G}_{xy} \bar{\mathbf{a}} \bar{\nabla}_{\mathrm{H}} h) \tag{18}$$

where $\bar{\mathbf{U}}^*$ is the effective contravariant velocity of the transformed space (e.g. a composition of the horizontal counterparts of the transformations (6) and (4)), and $\bar{\mathbf{a}}$ symbolizes the conjugate metric tensor of the transformed space, cf. Section 3.3 in Reference [15].

## 3. NUMERICAL MODEL

### *3.1. Flow solver*

The incompressible Boussinesq equations (2) and (3) are solved numerically using a second-order-accurate nonoscillatory forward-in-time (NFT) approach, broadly documented in the literature (see Reference [11, Section 4] for the principles of the formulation and Reference [30] for a succinct review). Below we comment briefly on the essential aspects of the numerical solution procedure while referring the reader to earlier works for further details.

 

Given (5), the evolution equation (3) for each velocity component can be written as an Eulerian conservation law

$$\frac{\partial \rho^* \psi}{\partial \bar{t}} + \bar{\nabla} \bullet (\bar{\mathbf{V}}^* \psi) = \rho^* R \tag{19}$$

where $\psi$ symbolizes components of $\mathbf{v}$, $\bar{\mathbf{V}}^* \equiv \rho^* \bar{\mathbf{v}}^*$, and $R$ denotes the associated rhs. An NFT algorithm employed to integrate (19) to second-order accuracy can be concisely written as

$$\psi_{\mathbf{i}}^{n+1} = \frac{\rho^{*n}}{\rho^{*n+1}} \mathscr{A}_{\mathbf{i}}(\tilde{\psi}, \bar{\mathbf{V}}^{*n+1/2}, \delta t) + 0.5 \delta t R_{\mathbf{i}}^{n+1} \tag{20}$$

where $\psi_{\mathbf{i}}^{n+1}$ is the solution sought at the grid point $(\bar{t}^{n+1}, \bar{\mathbf{x}}_{\mathbf{i}})$, $\tilde{\psi} \equiv \psi^n + 0.5 \delta t R^n$, and $\mathscr{A}$ denotes a two-time-level nonoscillatory flux-form transport operator [31]. Here, we use for $\mathscr{A}$ a fully second-order-accurate multidimensional MPDATA advection scheme [11, 30, 32]. Advecting velocity components with momenta (rather than the opposite) benefits the accuracy of incompressible-flow solvers. In particular, linearly extrapolated $\bar{\mathbf{V}}^{*n+1/2}$ assures that the advecting flow satisfies discrete mass continuity equation (2) to round-off error, and that the first-order truncation error terms proportional to $\partial \bar{\mathbf{V}}^* / \partial t$ vanish; cf. Reference [11] for discussion.

Subgrid-scale forcings (SGS) included in $R$ are evaluated explicitly and to the first-order. This is justified because they enter the equations of motion only as a consequence of a subgrid-scale turbulence model, already as $\sim \mathcal{O}(\delta x^2)$ corrections. Technically, this eliminates the need for predicting $\mathrm{SGS}^{n+1}$ in $R^{n+1}$ on the rhs of (20), as $\mathrm{SGS}(\psi^{n+1}) = \mathrm{SGS}(\psi^n) + \mathcal{O}(\delta t)$. Programming wise, the definition of the auxiliary field $\tilde{\psi}$ is expanded as $\tilde{\psi} \equiv \psi^n + 0.5 \delta t (R_{\mathrm{inv}}^n + 2 R_{\mathrm{sgs}}^n)$, while accounting only for the resolved inviscid forcing $R_{\mathrm{inv}}$ in $R^{n+1}$ on the rhs of (20); cf. Sections 3.5.4 and 4.2 in Reference [32] for discussion. The explicit first-order evaluation of SGS forcings improves the efficacy of calculations. When required however, it can be extended to the trapezoidal integral, employed for the inviscid forcing $R_{\mathrm{inv}}$, by means of an outer iteration scheme [33].

Equation (20) represents an implicit system, because velocity components and pressure are unknown at $t^{n+1}$. It can be written compactly as

$$\mathbf{v}_{\mathbf{i}} = \hat{\mathbf{v}}_{\mathbf{i}} - 0.5 \delta t (\tilde{\mathbf{G}} \bar{\nabla} \pi')_{\mathbf{i}} \tag{21}$$

where $\hat{\mathbf{v}}$ denotes the explicit counterpart of (20), and the superscript $n+1$ has been dropped as there is no ambiguity. On grids unstaggered with respect to all prognostic variables, (21) can be manipulated locally to construct expressions for the solenoidal velocity components that are subsequently substituted into discrete form of (2) to produce

$$\left[ \frac{\delta t}{\rho^*} \bar{\nabla} \bullet \rho^* \tilde{\mathbf{G}}^{\mathrm{T}} (\hat{\mathbf{v}} - 0.5 \delta t \tilde{\mathbf{G}} \bar{\nabla} \pi') \right]_{\mathbf{i}} = 0 \tag{22}$$

i.e. an elliptic equation for renormalized pressure $\pi''$

$$\left[ \frac{\delta t}{\rho^*} \bar{\nabla} \bullet \rho^* \tilde{\mathbf{G}}^{\mathrm{T}} (\hat{\mathbf{v}} - \tilde{\mathbf{G}} \bar{\nabla} \pi'') \right]_{\mathbf{i}} = 0 \tag{23}$$

where $\hat{\mathbf{v}} - \tilde{\mathbf{G}} \bar{\nabla} \pi'' \equiv \bar{\mathbf{v}}^{\mathrm{s}}$ defined in (4); cf. Reference [13] for the complete development. Boundary conditions imposed on $\bar{\mathbf{v}}^{\mathrm{s}} \bullet \mathbf{n}$, subject to the integrability condition $\int_{\partial \Omega} \rho^* \bar{\mathbf{v}}^{\mathrm{s}} \bullet \mathbf{n} \, \mathrm{d}\sigma = 0$,

 

imply the appropriate boundary conditions on $\tilde{\mathbf{G}}\,\bar{\nabla}\pi'' \bullet \mathbf{n}$ [13, 14]. The resulting boundary value problem is solved using a preconditioned generalized conjugate residual GCR($k$) algorithm, a nonsymmetric Krylov subspace solver akin to the popular generalized minimum residual GMRES($k$) scheme [34–38]. Given the updated pressure, and hence the updated solenoidal velocity, the updated physical and contravariant velocity components are constructed from the solenoidal velocities using transformations (6) and (4), respectively.

### 3.2. Sediment transport

The metric and transformation coefficients embedded in (2) and (3) as well as the time derivative of the transformed coordinates in (4) enter the solution procedure at $t^{n+1}$ via $R^{n+1}$ term on the rhs of (20) as well as the coefficients and boundary conditions of the elliptic problem (23). They are supplied by integrating the advection–diffusion PDE (18) over the double time step of the fluid model (effectively, from $t^n$ to $t^{n+2}$) and then centering $h$ and $\partial h/\partial t$ at $t^{n+1}$; the results were found insensitive to variations in time stepping. Consistent with the fluid model, the sediment-transport model (18) is integrated explicitly to $\mathcal{O}(\delta t^2)$, using the NFT scheme

$$h_{\mathbf{j}}^{n+2} = \frac{\overline{G_{xy}}^{n}}{\overline{G_{xy}}^{n+2}}\,\mathscr{A}_{\mathbf{j}}(\tilde{h},\, \bar{\mathbf{U}}^{*n}, 2\delta t) \tag{24}$$

Here, $\mathscr{A}_{\mathbf{j}}$ refers to a nonoscillatory horizontal-advection operator,[‖] and $\tilde{h} \equiv h^n + 2\delta t\,\mathscr{L}(\mathscr{K}^n, h^n)$, with $\mathscr{L}$ symbolizing the generalized Laplacian on the rhs of (18), for all horizontal grid points $\mathbf{j} = (i, j)$. Integrating (18) to first order suffices for a second-order accuracy of the fluid model.

Due to discrete truncation, casting the saltation flux in (11) as an advective flux in (18), via (17), can violate the boundedness of the resulting Courant number, locally as $h \searrow 0$ reaching the upper limit of nonerodible substrate; cf. discussion following (17). The latter admits negative values of $h$, even with a sign-preserving advection scheme employed in (24).[**] As $h$ becomes negative, the local Courant numbers can amplify, effecting ultimately in computational instability of the sediment motion model. A number of finite-difference approximations to (17) may be conceived to address this subtle stability issue. Here, we adopt a general approach applicable with any transport scheme employed in (24). First, we evaluate (17) at the cell walls straightforwardly, with disregard to the stability issue; for instance, in the spirit of standard centred approximations

$$UX_{i+1/2,j} = \frac{1}{\rho_{\mathrm{s}}}\,\frac{qx_{i+1/2,j} + qx_{i,j}}{h_{i+1/2,j} + h_{i,j}} \tag{25}$$

where only a Cartesian case is highlighted for illustration, so that $qx$ refers to the $x$ component of the saltation flux. Second, to prevent negative $h$, we limit advective fluxes in (24) using the multidimensional flux-limiter—Equation (10) in Section 3b of Reference [39], a special case of general flux-corrected approach [40]—that assures nonnegative $\tilde{h}$ in (24), consistent with physical character of (18). Notably, there is no need to limit the fluxes for dunes evolving on a

[‖] The first-order-accurate MPDATA option, viz. the donor-cell scheme, has been used in this study.

[**] Recall that MPDATA schemes are sign-preserving given properly bounded Courant numbers; cf. Reference [11] for discussion.

 

substantial erodible bed. Consequently, the magnitude of undershoots spurious for nonerodible beds may be assessed *a posteriori* from the erodible-bed experiments, e.g. compare Figures 2 and 4 discussed in Section 4.2.

## 4. NUMERICAL SIMULATIONS

### *4.1. Design of experiments*

We consider a neutrally stratified, nonrotating Boussinesq atmosphere with uniform ambient wind $\mathbf{v}_e = (11, 0, 0)\ \mathrm{m\,s^{-1}}$; and specify a Cartesian model domain $L_x \times L_y \times L_z = 340 \times 180 \times 40\ \mathrm{m}^3$, a compromise between the requirements of the flow resolution and the processor array distribution of massively parallel computations. For the lower boundary at $t = 0$, we select a cosine sandpile of height $h_o = 7.5$ m and the half-width $a = 50$ m, centred at $(x_o, y_o) = (L_x/3, L_y/2)$

$$h(\mathbf{x}, t=0) = \begin{cases} h_o \cos^2\left(\dfrac{\pi r}{2a}\right) + h_\mathrm{b} & \text{if } r/a \leqslant 1 \\ h_\mathrm{b} & \text{if } r/a > 1 \end{cases} \tag{26}$$

where $r \equiv \sqrt{(x - x_o)^2 + (y - y_o)^2}$. In (26), $h_\mathrm{b}$ denotes the thickness of the sand layer underneath the pile (bed), selected either 0 or 5 m in the experiments discussed here.

The key premise of this study is the 'severe wind scenario' that shrinks the gap between the time scales characteristic of planetary boundary layer flows $\mathcal{O}(10^3)$ s and sand dune evolution $\mathcal{O}(10^6)$ s. Here, this is realized by rescaling the empirical coefficient $C = 5.5$ in (12) by the factor of 1440 (minutes per day).[††] This is expected to have a similar impact on the solution as reducing the gravity (e.g. via posing the problem on a tenfold smaller planet), increasing the fluid density (e.g. from air to water), or amplifying the ambient wind ten times. The latter is computationally most stringent, as it severely limits the temporal integration increment $\delta t$. With the rescaled saltation flux, the model equations are integrated over several characteristic times $T = 10^3$ s, each corresponding to $\sim 30$ advection time scales $L_x/u_e$. The equations are solved on a regular mesh (in the transformed space) consisting of $171 \times 91 \times 41$ grid points with $\delta t = 0.05$ s. For the upper boundary the rigid lid is assumed, whereas lateral boundaries incorporate open and periodic boundary conditions in the streamwise and spanwise directions, respectively. The initial condition assumes the potential flow.

The remaining simulation parameters are as follows. The surface drag coefficient in the Smagorinsky-type turbulence subgrid-scale model [17] is $C_\mathrm{D} = 0.01$; the spatial and temporal scales that enter the avalanche flux via (15) are selected as $\Lambda = 0.25 \min(\delta x, \delta y)$ and $\Upsilon = \delta t$.[‡‡] The friction velocity $\mathbf{u}_*$ is evaluated from the logarithmic law

$$\mathbf{u}_* = \kappa \frac{(\mathbf{v} - \mathbf{v} \bullet \mathbf{n})|_{z_\Delta}}{\ln(z_\Delta / z_0)} \tag{27}$$

[††] After Lettau and Lettau [23], $C = 5.5$ corresponding to the standard grain size $0.25 \times 10^{-3}$ m is typically assumed in the literature [2, 5, 7].

[‡‡] The choice of the avalanche scales $\Lambda$ and $\Upsilon$ compromises our own observations, cf. Figure 1, and numerical stability arguments; our measurements indicate $\Lambda \in [0.3, 3]$ m, and $\Lambda/\Upsilon \approx 0.3\ \mathrm{m\,s^{-1}}$.

 

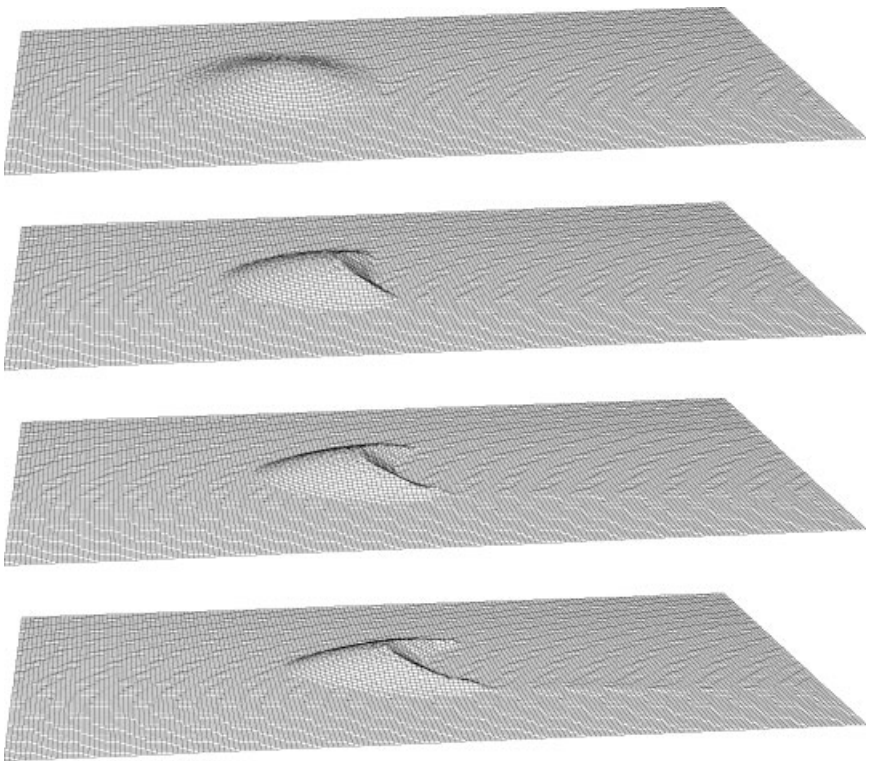

Figure 2. Evolution of a barchan dune; surface shape.

where $z_\Delta$ is the distance between the surface and the adjacent model level, cf. Reference [7], and $z_0$ is an equivalent roughness length (accounting for the flow-to-grains momentum transfer) taken as $z_o = 0.001$ m, and $\kappa = 0.41$ is the von Karman constant. The sediment transport parameters are: $\rho_m = 2650\ \mathrm{kg/m^3}$ for the density of quartz, $\lambda = 0$ for the porosity; and the horizontal threshold friction velocity is $u_{\tau 0} = 0.22\ \mathrm{m\,s^{-1}}$, corresponding to the the standard grain size $0.25 \times 10^{-3}$ m [23].

### 4.2. Results

The development of an isolated barchan dune placed on a nonerodible bed is a canonical problem in the study of evolutionary sand dune dynamics [5, 7, 21, 24] and, as mentioned in Section 1, still eludes complete understanding. Figure 2 displays the transformation of the initial sandpile into a barchan dune over 72 min of our model simulation, at 24 min intervals; whereas Figure 3 shows the developed boundary layer flow (isolines of vertical velocity and flow vectors), in the central vertical plane and at the lower surface, respectively, superimposed with the dune altitude profile, at 84 min of the simulated time. The apparent break of the solution symmetry is attributed to the accumulation of round-off error over $\mathcal{O}(10^5)$ time steps, accentuated by the nonlinearity of the atmosphere/dune coupling.

 

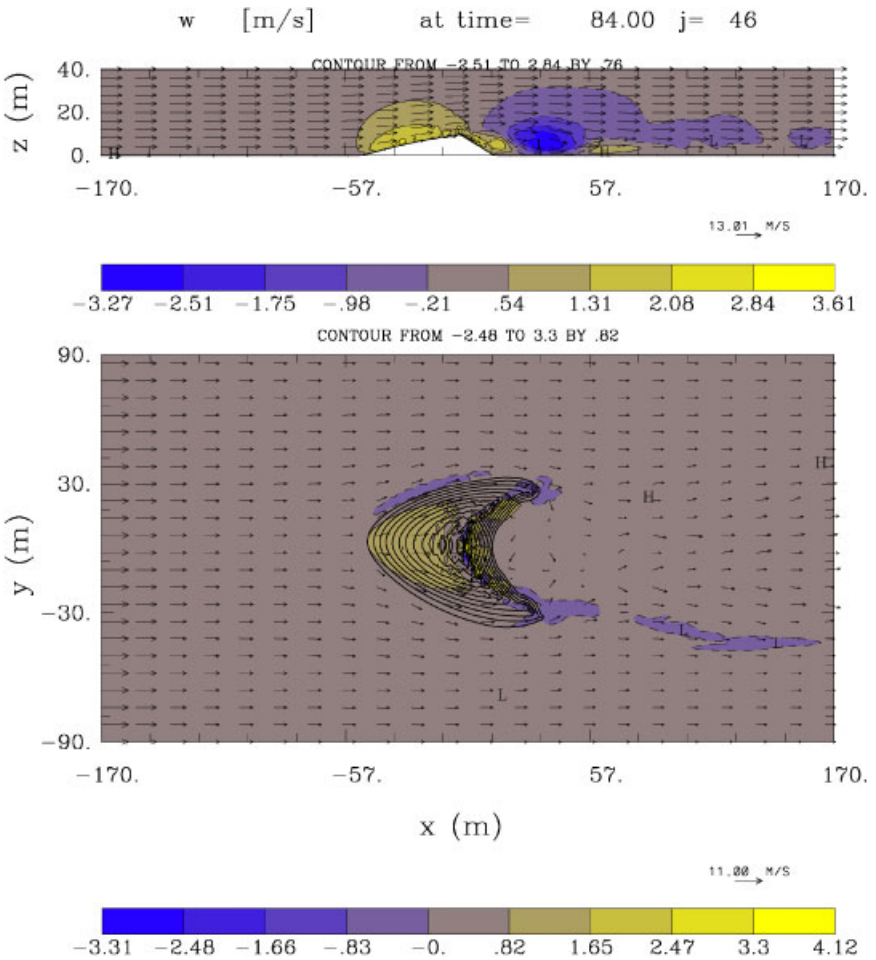


Figure 3. Vertical velocity in the central $xz$ plane and at the surface, at 84 min of simulated time. The superimposed isolines of the surface height are plotted with contour interval $0.1h_o$.

The highlighted results fall in the range obtained in other computational studies. For instance, our average propagation speed 0.8 m/mn is, after rescaling while accounting for more standard porosity $\lambda = 0.5$, roughly half of that reported in Reference [7] and close to value quoted in Reference [5]. Furthermore, it is on the order of the values measured for small barchan dunes in Reference [24]. Another example is the length of horns after shape stabilization, equal to about 5–6 dune heights in our experiments, compared to 9 heights measured in the Arequipa region (Southern Peru) [24]. Since in all studies there are discrepancies in the initial, boundary, and ambient conditions, the overall agreement of the results is encouraging.

Together, Figures 2 and 3 demonstrate that the simulated dune is defined always over compact support, free of sand residual trailing on the windward side. This is different from the results discussed in the literature that report unphysical sand deposition at the windward

 

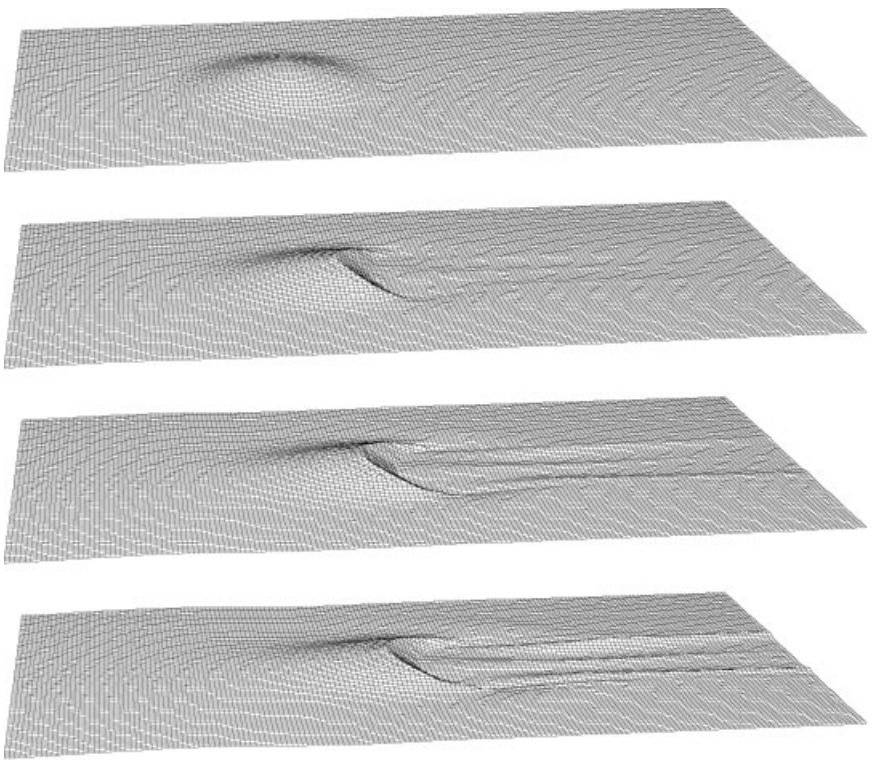

Figure 4. Evolution of a barchan dune with a sand bed beneath; surface shape.

foot of the dune. This effect is often attributed to the saturation model (12). The authors [5] (see their Section 3.2) argue that the incompressible mass continuity equation inevitably leads to the positive $\partial h/\partial t$ at the windward side. Since our saltation model is, in essence, the same as those used in earlier works, we infer that our successful prediction is related to the full coupling of both phases of the two-fluid model. In particular, the time dependency of our mass continuity equation (5), augments the arguments of Weng *et al.* [5] by incorporating the additional term $\propto \partial h/\partial t$ that counterbalances the tendency for the negative horizontal divergence on the windward side of the dune. Effectively, this makes problem (18) implicit in $\partial h/\partial t$, with the saturation flux depending not only on $h$ but also on its time derivative.

Figures 4 and 5 display solutions equivalent to those in Figures 2 and 3, except for the 5 m deep erodible bed incorporated underneath the initial sand pile. The principal dune evolves similarly to the nonerodible-bed case, with apparent differences in the lee reflecting the saltation-flux response to the separated wake flow. A closer examination of the results reveals that there is also a subtle difference on the windward side. The solution in Figures 4 and 5 evinces a sand deposition gently trailing along the symmetry axis upwind of the dune, with descending slopes at the lateral sides of the dune. This low amplitude large-scale waviness of the surface profile is consistent with the simulated boundary layer flow. From (11), (12), and (27), it follows that $\partial h/\partial t \sim -\partial u/\partial x$. As the incoming flow decelerates in response to surface friction, $\partial h/\partial t > 0$ forming an ascending slope. As flow trajectories

 

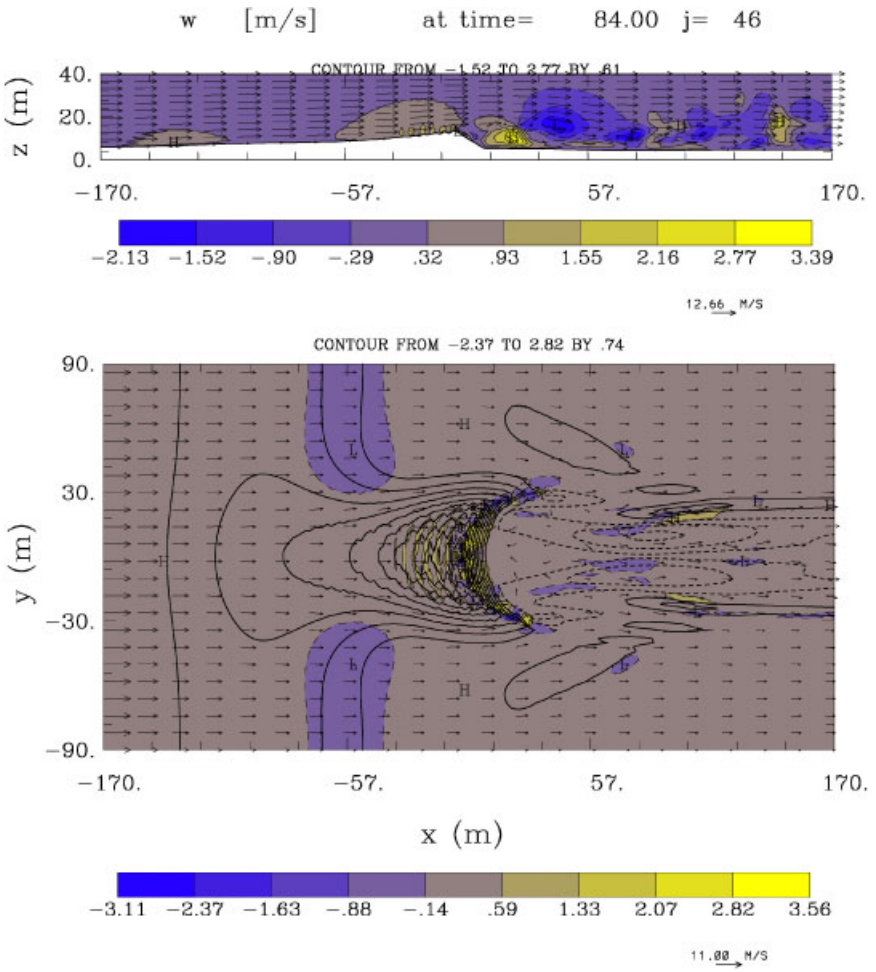


Figure 5. Barchan dune with a sand bed: vertical velocity in the central *xz* plane and at the surface at 84 min of simulated time.

approach the dune, deflect to the sides, and the surface wind accelerates, $\partial h/\partial t < 0$ thus forming a descending slope. These weak effects are anticipated to be sensitive to the assumed initial wind profile as well as the inflow and lateral boundary conditions. In other words, if they are judged spurious then they call for more realistic setups of the numerical experiment, rather than indicating an inadequacy of either a sediment-transport or fluid model *per se*.

## 5. CONCLUDING REMARKS

Predicting sediment transport and bed evolution in severe wind conditions depends on accurate prediction of flow past a complex boundary evolving with the flow itself. The

 

geometrical complexity of the evolving interfaces—which either accommodate dynamically to the external/internal boundaries of the domain, or convolute in response to internal flows—is *per se* a challenge to numerical modelling. In this paper, we have developed a variant of the nonhydrostatic model EULAG that couples the atmospheric flow with a lower boundary evolving in response to the sand saltation. The key prerequisite facilitating this development is the use of a time-dependent curvilinear coordinate transformation that accommodates rapid changes of the boundary shape. The nonoscillatory forward-in-time numerical technology of EULAG enables novel numerical designs that improve the accuracy, stability, and robustness of the traditional saltation models that govern the evolution of dunes.

The key premise of our development is the 'severe wind scenario' that shrinks the gap between the time scales characteristic of planetary boundary layer flows and sand dune evolution by three orders of magnitude. Here, it is realized by rescaling the empirical coefficient $C$ in the saturation model (12) by a factor of 1440 (minutes per day). Arguably, this has a similar impact on the solution as reducing the gravity (e.g. via posing the problem on a tenfold smaller planet), increasing the fluid density (e.g. from air to water), or amplifying the ambient wind ten times. The latter is computationally least attractive, as it severely limits the temporal integration increment. With the rescaled saltation flux, the two-phase model equations can be integrated consistently and efficiently, while simplifying the programming efforts associated with the phase coupling. The resulting model dispenses with quasi-steady approximation and scale-separation assumption, thereby enabling numerical investigations of sand dune evolutions from first principles, in the spirit of idealized laboratory studies.

To simplify and focus the presentation of the two-phase model and associated computational procedures, here, we only considered a shallow flow of thermally homogeneous planetary boundary layer, adopting the classical incompressible Boussinesq approximation in the governing fluid equations. The latter invokes only a small portion of the model capabilities. The nonhydrostatic anelastic model EULAG—the mathematical/numerical foundation of the present two-phase system—has been proven successful in simulating rotating, stratified, thermally forced flows in complex geometries, on scales from micro to planetary [30]. Consequently, the developments presented in this paper extend readily to a broad range of sediment transport problems on scales from micro to planetary.

## APPENDIX A

The dependence of the threshold friction velocity, $u_t$ in (12), on the landform slope has been addressed for slab symmetry [25]. In 3D applications, it is important to account for the nonalignment of the local maximum slope and wind direction. Following Reference [26], we proceed assuming the equality of tractive force and friction as well as the independence of the drag coefficient on the slope magnitude.

Consider a grain particle at a point on the sloped surface, and the forces of gravity $\mathbf{W}$ and the fluid drag $\mathbf{D}$ acting on it. Decomposing $\mathbf{W}$ into the normal $|\mathbf{W}|\cos\theta$ and the tangential $|\mathbf{W}|\sin\theta$ in the direction of the maximal local slope, the tractive force $\mathbf{F}$ is the resultant of $\mathbf{D}$ and $|\mathbf{W}|\sin\theta$. The critical condition for the onset of motion is traction equal friction,

 

i.e. $|\mathbf{F}| = |\mathbf{W}| \cos\theta \cdot \tan\alpha$, where $\alpha$ is the angle of friction. The resultant force

$$\mathbf{F} = \left( -\frac{|\mathbf{W}| \sin\theta}{|\nabla h|} \frac{\partial h}{\partial x} + |\mathbf{D}| \frac{u}{|\mathbf{v}|} \right) \mathbf{i} + \left( -\frac{|\mathbf{W}| \sin\theta}{|\nabla h|} \frac{\partial h}{\partial y} + |\mathbf{D}| \frac{v}{|\mathbf{v}|} \right) \mathbf{j} + \left( -\frac{|\mathbf{W}| \sin\theta}{|\nabla h|} + |\mathbf{D}| \frac{w}{|\mathbf{v}|} \right) \mathbf{k} \tag{A1}$$

comprises components $u, v, w$ of the flow velocity $\mathbf{v}$, tangential in the vicinity of surface due to the impermeability boundary condition $\mathbf{v} \cdot \mathbf{n} = 0|_{\tilde{z}=0}$ imposed.

The critical condition for a horizontal bed ($\theta = 0$)

$$|\mathbf{D}_0| = |\mathbf{W}| \tan\alpha \tag{A2}$$

relates the particle weight to the critical drag for flat surface, $\mathbf{D}_0$, and the friction angle; whereas the assumption of the drag coefficient independence on the slope results in

$$\frac{\mathbf{D}}{\mathbf{D}_0} = \frac{u_\mathrm{t}^2}{u_{\mathrm{t}0}^2} \tag{A3}$$

Substituting (A2) and (A3) in (A1) leads to the quartic equation for the normalized friction threshold velocity $u_\mathrm{t}/u_{\mathrm{t}0}$

$$\left( \frac{u_\mathrm{t}^2}{u_{\mathrm{t}0}^2} \cdot \frac{u}{|\mathbf{v}|} - \frac{\sin\theta}{\tan\alpha} \frac{\partial h}{\partial x} \frac{1}{|\nabla h|} \right)^2 + \left( \frac{u_\mathrm{t}^2}{u_{\mathrm{t}0}^2} \cdot \frac{v}{|\mathbf{v}|} - \frac{\sin\theta}{\tan\alpha} \frac{\partial h}{\partial y} \frac{1}{|\nabla h|} \right)^2 + \left( \frac{u_\mathrm{t}^2}{u_{\mathrm{t}0}^2} \cdot \frac{w}{|\mathbf{v}|} - \frac{\sin\theta}{\tan\alpha} \frac{1}{|\nabla h|} \right)^2 = \cos^2\theta \tag{A4}$$

Note that $|\nabla h| > 0$ and $\tan\alpha > 0$, always and everywhere. Furthermore, all coefficients in (A4) are bounded when $|\mathbf{v}| \searrow 0$. Solving (A4) for $u_\mathrm{t}^2/u_{\mathrm{t}0}^2$ leads to (13), where all terms dependent on flow direction collapse into $\cos\gamma$.

To appreciate the importance of the slope correction, consider the asymptotic limits, within the $0 \leqslant \theta \leqslant \alpha$ and $0 \leqslant \gamma \leqslant \pi$ bounds. For $\theta \neq 0$ and $\gamma = 0$, the multiplicative factor in (13) varies between 1 (for $\theta = 0$) and 1.7 (for $\theta = \alpha$). For $\theta \neq 0$ and $0 < \gamma < \pi/2$, the correction factor decreases for increasing $\gamma$ nearly to 1.0 for gentle slopes, and nearly to zero when the slope approaches the critical and $\gamma \approx \pi/2$. For $\theta \neq 0$ and $\gamma = \pi/2$, the factor varies from 1.0 for $\theta = 0$ to 0.1 for $\theta \approx \alpha$. When $\theta \neq 0$ and $\pi/2 \leqslant \gamma \leqslant \pi$, the correction factor is smaller than unity and decreases with increasing $\gamma$, while for $\theta \approx 0$ goes to nearly zero.

ACKNOWLEDGEMENTS

Personal review by Robert Sharman is gratefully acknowledged. We thank Nils Wedi for his assistance with measurements of sand avalanches, and Andrzej Wyszogrodzki for his help with parallelizing the sediment-transport module of the model. This work was supported in part by the U.S. Department of Energy 'Climate Change Prediction Program' (CCPP) research initiative.

 

REFERENCES


1. Werner BT. Eolian dunes: computer simulations and attractor interpretation. *Geology* 1995; **23**:1107–1110.
2. Nishimori H, Yamasaki M, Andersen KA. A simple model for the various pattern dynamics of dunes. *International Journal of Modern Physics B* 1998; **12**:257–272.
3. Venditti JG, Bennett SJ. Spectral analysis of turbulent flow and suspended sediment transport over fixed dunes. *Journal of Geophysical Research* 2000; **105**(C9):22,035–22,047.
4. Momiji H, Carretero-González R, Bishop SR, Warren A. Simulation of the effect of wind speedup in the formation of transverse dune fields. *Earth Surface Processes and Landforms* 2000; **25**:905–918.
5. Weng WS, Hunt JCR, Carruthers DJ, Warren A, Wiggs GFS, Livingstone I, Castro I. Air flow and sand transport over sand-dunes. *Acta Mechanica* 1991; **2**(Suppl):1–22.
6. Schwämmle V, Herrmann HJ. Modelling transverse dunes. *Earth Surface Processes and Landforms* 2004; **29**:769–784.
7. Wippermann FK, Gross G. The wind-induced shaping and migration of an isolated dune: a numerical experiment. *Boundary Layer Meteorology* 1986; **36**:319–334.
8. Howard AD, Morton JB, Gad-El-Hak M, Pierce DB. Sand transport model of barchan dune equilibrium. *Sedimentology* 1978; **25**:307–338.
9. Shao Y. *Physics and Modelling of Wind Erosion*. Kluwer Academic Publishers: Dordrecht, 2000.
10. Herrmann HJ, Sauermann G. The shape of dunes. *Physica A* 2000; **283**:24–30.
11. Smolarkiewicz PK. Multidimensional positive definite advection transport algorithm: an overview. *International Journal for Numerical Methods in Fluids* 2005; *ibid.*
12. Prusa JM, Smolarkiewicz PK, Garcia RR. On the propagation and breaking at high altitudes of gravity waves excited by tropospheric forcing. *Journal of the Atmospheric Sciences* 1996; **53**:2186–2216.
13. Prusa JM, Smolarkiewicz PK. An all-scale anelastic model for geophysical flows: dynamic grid deformation. *Journal of Computational Physics* 2003; **190**:601–622.
14. Wedi NP, Smolarkiewicz PK. Extending Gal-Chen and Somerville terrain-following coordinate transformation on time dependent curvilinear boundaries. *Journal of Computational Physics* 2004; **193**:1–20.
15. Smolarkiewicz PK, Prusa JM. Towards mesh adaptivity for geophysical turbulence. *International Journal for Numerical Methods in Fluids* 2005; **47**:789–801.
16. Prusa JM, Gutowski WJ. MPDATA and grid adaptivity in geophysical fluid flow models. *International Journal for Numerical Methods in Fluids* 2005; *ibid.*
17. Margolin LG, Smolarkiewicz PK, Sorbjan Z. Large-eddy simulations of convective boundary layers using nonoscillatory differencing. *Physica D* 1999; **133**:390–397.
18. Sauermann G, Kroy K, Herrmann HJ. Continuum saltation model for sand dunes. *Physical Review E* 2001; **64** 031305:1–10.
19. Prigozhin L, Zaltzmann B. Two continuous models for the dynamics of sandpiles surfaces. *Physical Review E* 2001; **63** 041505:1–6.
20. Prusa JM, Smolarkiewicz PK, Wyszogrodzki AA. Simulations of gravity wave induced turbulence using 512 PE CRAY T3E. *International Journal of Applied Mathematics and Computer Science* 2001; **11**(4):101–115.
21. Bagnold RA. *The Physics of Blown Sand and Desert Dunes*. Methuen: London, 1941.
22. Bouchaud JP, Cates ME, Ravi Prakash J, Edwards SF. Hysteresis and metastability in a continuum sandpile model. *Physical Review Letters* 1995; **74**(11):1982–1985.
23. Lettau K, Lettau HH. Experimental and micro-meteorological field studies of dune migration. In *Exploring the Worlds Driest Climate*, Lettau HH, Lettau K (eds), Center for Climatic Research, University of Wisconsin, Madison, 1978.
24. Andreotti B, Claudin P, Douady S. Selection of dune shapes and velocities. Part 1: dynamics of sand, wind and barchans. *European Physical Journal B* 2002; **28**:321–340.
25. Iversen JD, Rasmussen KR. The effect of surface slope on saltation threshold. *Sedimentology* 1994; **41**:721–728.
26. Brooks NH. Boundary shear stresses in curved trapezoidal channels: a discussion. *ASCE Proceedings* 1963; **89**(HY3):327–333.
27. Gillette DA, Adams J, Muhs D, Kihl R. Threshold friction velocities and rupture moduli for crusted desert soils for the input of soil particles into the air. *Journal of Geophysical Research* 1982; **87**(C11):9003–9015.
28. Bak P, Tang Ch, Wiesenfeld K. Self-organized criticality. *Physical Review A* 1987; **38**(1):364–374.
29. Jaeger H, Chu-heng L, Nagel S. Relaxation at the angle of repose. *Physical Review Letters* 1989; **62**:40–43.
30. Smolarkiewicz PK, Prusa JM. Forward-in-time differencing for fluids: simulation of geophysical turbulence. In *Turbulent Flow Computation*, Drikakis D, Guertz BJ (eds). Kluwer Academic Publishers: Dordrecht, 2002; 279–312.
31. Smolarkiewicz PK, Margolin LG. On forward-in-time differencing for fluids: extension to a curvilinear framework. *Monthly Weather Review* 1993; **121**:1847–1859.
32. Smolarkiewicz PK, Margolin LG. MPDATA: a finite-difference solver for geophysical flows. *Journal of Computational Physics* 1998; **140**:459–480.


 

33. Cotter CS, Smolarkiewicz PK, Szczyrba IN. A viscoelastic model for brain injuries. *International Journal for Numerical Methods in Fluids* 2002; **40**:303–311.
34. Eisenstat SC, Elman HC, Schultz MH. Variational iterative methods for nonsymmetric systems of linear equations. *SIAM Journal on Numerical Analysis* 1983; **20**:345–357.
35. Saad Y. A flexible inner-outer preconditioned GMRES algorithm. *SIAM Journal on Scientific and Statistical Computing* 1993; **14**:461–469.
36. Smolarkiewicz PK, Margolin LG. Variational solver for elliptic problems in atmospheric flows. *Applied Mathematics and Computer Science* 1994; **4**:527–551.
37. Smolarkiewicz PK, Grubišić V, Margolin LG. On forward-in-time differencing for fluids: stopping criteria for iterative solutions of anelastic pressure equations. *Monthly Weather Review* 1997; **125**:647–654.
38. Skamarock WC, Smolarkiewicz PK, Klemp JB. Preconditioned conjugate-residual solvers for Helmholtz equations in nonhydrostatic models. *Monthly Weather Review* 1997; **125**:587–599.
39. Smolarkiewicz PK. Comment on 'A positive definite advection scheme obtained by nonlinear renormalization of the advective fluxes'. *Monthly Weather Review* 1989; **117**:2626–2632.
40. Smolarkiewicz PK, Grabowski WW. The multidimensional positive definite advection transport algorithm: nonoscillatory option. *Journal of Computational Physics* 1990; **86**:355–375.

 